

# Comparison between lidar and nephelometer measurements of aerosol hygroscopicity at the Southern Great Plains Atmospheric Radiation Measurement site

M. Pahlow,<sup>1</sup> G. Feingold,<sup>1</sup> A. Jefferson,<sup>2</sup> E. Andrews,<sup>2</sup> J. A. Ogren,<sup>2</sup>

J. Wang<sup>3</sup> Y.-N. Lee<sup>3</sup> and R. A. Ferrare<sup>4</sup>

---

M. Pahlow, NOAA, Environmental Technology Laboratory 325 Broadway, Boulder, Colorado 80305. (e-mail: Markus.Pahlow@noaa.gov)

G. Feingold, NOAA, Environmental Technology Laboratory 325 Broadway, Boulder, Colorado 80305. (e-mail: Graham.Feingold@noaa.gov)

A. Jefferson, NOAA, Climate Monitoring and Diagnostics Laboratory 325 Broadway, Boulder, Colorado 80305. (e-mail: Anne.Jefferson@noaa.gov)

E. Andrews, NOAA, Climate Monitoring and Diagnostics Laboratory 325 Broadway, Boulder, Colorado 80305. (e-mail: Betsy.Andrews@noaa.gov)

J. A. Ogren, NOAA, Climate Monitoring and Diagnostics Laboratory 325 Broadway, Boulder, Colorado 80305. (e-mail: John.A.Ogren@noaa.gov)

J. Wang, Brookhaven National Laboratory, Upton, New York, USA (e-mail: Jian@bnl.gov)

Y.-N. Lee, Brookhaven National Laboratory, Upton, New York, USA (e-mail: Ynlee@bnl.gov)

R. A. Ferrare, NASA, Langley Research Center, Hampton, Virginia, USA (e-mail: Richard.A.Ferrare@nasa.gov)

<sup>1</sup>NOAA, Environmental Technology Laboratory, Boulder, CO 80305.

<sup>2</sup>NOAA, Climate Monitoring and Diagnostics Laboratory, Boulder, CO 80305.

<sup>3</sup>Brookhaven National Laboratory, Upton, New York, USA.

<sup>4</sup>NASA, Langley Research Center, Hampton, Virginia, USA.

**Abstract.**

Aerosol hygroscopicity has a significant effect on radiative properties of aerosols. Here a lidar method, applicable to cloud-capped, well-mixed atmospheric boundary layers, is employed to determine the hygroscopic growth factor  $f(\text{RH})$  under unperturbed, ambient atmospheric conditions. The data used for the analysis were collected under a wide range of atmospheric aerosol levels during both routine measurement periods and during the intensive operations period (IOP) in May 2003 at the Southern Great Plains (SGP) Climate Research Facility in Oklahoma, USA, as part of the Atmospheric Radiation Measurement (ARM) program. There is a good correlation ( $\sim 0.7$ ) between a lidar-derived growth factor (measured over the range 85% RH to 96% RH) with a nephelometer-derived growth factor measured over the RH range 40% to 85%. For these RH ranges, the slope of the lidar-derived growth factor is much steeper than that of the nephelometer-derived growth factor, reflecting the rapid increase in particle size with increasing RH. The results are corroborated by aerosol model calculations of lidar and nephelometer equivalent  $f(\text{RH})$  based on *in situ* aerosol size and composition measurements during the IOP. It is suggested that the lidar method can provide useful measurements of the dependence of aerosol optical properties on relative humidity, and under conditions closer to saturation than can currently be achieved with humidified nephelometers.

## 1. Introduction

The importance of atmospheric aerosols for the Earth’s climate has been widely recognized [e.g. *Charlson et al.*, 1992; *Boucher and Anderson*, 1995; *Vogelmann et al.*, 2003]. They affect solar radiation and hence climate directly by scattering radiation back to space [*Charlson et al.*, 1992], but also indirectly by acting as cloud condensation nuclei [*Twomey*, 1974]. An important factor affecting the role aerosols play in climate change is their hygroscopicity. The swelling of aerosols due to water vapor uptake will enhance their ability to scatter radiation. Numerous studies have investigated the relationship between aerosol scattering and relative humidity RH in terms of the hygroscopic growth factor  $f(\text{RH})$  using humidified nephelometers. These have been used for airborne or ground-based determination of the growth factor considering a “dry” RH over the range 20%–40% and a “wet” RH up to 90% [e.g. *Covert et al.*, 1972; *McInnes et al.*, 1998; *Kotchenruther et al.*, 1999; *Malm et al.*, 2003]. Humidified Tandem Differential Mobility Analyzers (HTDMAs) allow one to determine aerosol hygroscopicity as a function of particle size, usually for RH up to  $\sim 90\%$  [e.g. *McMurry and Stolzenburg*, 1989; *Covert and Heintzenberg*, 1993; *Brechtel and Kreidenweis*, 2000]. The lidar (light detection and ranging) technique provides the opportunity to investigate hygroscopic growth of aerosols beyond this RH range, under ambient atmospheric conditions and without perturbing the sampled air. *Ferrare et al.* [1998] used Raman lidar to simultaneously measure aerosol backscatter and RH in a study that demonstrated the ability of lidar to measure  $f(\text{RH})$ . *Wulfmeyer and Feingold* [2000] used differential absorption lidar to measure the enhancement in backscatter in the regime of high RH up to  $\sim 98.5\%$ . More recently *Feingold and Morley* [2003] (henceforth FM) used elastic backscatter lidar data combined with thermodynamic assumptions of the mixing

state of the atmosphere to determine  $f(\text{RH})$  for RH up to  $\sim 98.5\%$ . In this paper we make use of this combined lidar-thermodynamic approach to determine  $f(\text{RH})$  for relative humidities close to saturation and for a broad range of atmospheric aerosol conditions. We apply this method for a much broader range of aerosol conditions than has been done in the past. The analysis by *Wulfmeyer and Feingold* [2000] was limited to a one-minute time period and FM analyzed 30 minutes worth of data. We also provide first comparisons with a ground-based nephelometer-derived  $f(\text{RH})$  and show that there is a strong correlation between these two independently derived growth factors. In addition, we show that there is broad consistency between lidar and nephelometer growth factors and those computed from *in situ* aerosol size distribution and composition measurements during the IOP.

## 2. Experiment

The data used for our analysis were collected between 1998 and 2003 during both routine measurement periods and the intensive operations period (IOP) in May 2003, at the Southern Great Plains (SGP) Climate Research Facility in Oklahoma, USA (latitude  $+36.605$ , longitude  $-97.489$ ; elevation: 315 m asl), as part of the Atmospheric Radiation Measurement (ARM) program. We utilize CART (Cloud and Radiation Testbed) Raman lidar data (355 nm), three wavelength (450 nm, 550 nm and 700 nm) nephelometer data (two TSI models 3563, one of them humidified - called a humidograph, sampling aerosol particles with a diameter of  $\leq 10 \mu\text{m}$ ), light absorption photometer data (Radiance Research model PSAP) adjusted to 550 nm by calibration corrections, as well as micrometeorological data. During the IOP we also use data from a differential mobility analyzer (DMA; TSI model 3081), tapered-element oscillating microbalance (TEOM; Rupprecht

and Patashnick Series 1400a) and a particle-into-liquid sampler with ion chromatography analysis (PILS-IC; *Orsini et al.*, 2003). The CART Raman lidar is a self-contained, fully computer-automated system designed for unattended, continuous profiling of water vapor, aerosols and clouds at the ARM SGP Climate Research Facility (*Goldsmith et al.*, 1998; *Turner et al.*, 2002). The light source is a frequency-tripled Nd:YAG laser, operating at 30 Hz with 400 millijoule pulses to transmit light at 355 nm. The vertical range resolution is 39 m and the time resolution is 10 minutes, after averaging. The light scattering (nephelometer) and absorption (light absorption photometer) measurements used here are one-hour averages. The humidograph data are collected over a  $\sim 1$ -hour period, during which the RH is increased from  $\sim 30\%$  to  $\sim 85\%$ . The DMA samples at 2 minute intervals over a particle size range from 27 nm to 815 nm. TEOM and PILS-IC are measured over 8 minute intervals and interpolated to 5 minute intervals. Supporting micrometeorological data (potential temperature  $\theta$  and specific humidity  $q$ ) are collected at one-minute intervals on a tower at a height of 60 m above ground level.

### 3. Method

To determine a growth factor  $f(\text{RH})_\beta$  from Raman lidar backscatter profiles and micrometeorological *in situ* data we employ thermodynamic assumptions for a cloud-capped, well-mixed boundary layer suggested by FM. For the approach to be applicable, the boundary layer must be well-mixed in potential temperature  $\theta$ , specific humidity  $q$ , and aerosol. When these criteria are met, the enhancement in backscatter with increasing vertical range is due to water vapor uptake, rather than to the existence of layers of aerosol or poorly defined RH. It is assumed that cloud base  $z_{cb}$  corresponds to 100% RH. Using an iterative procedure, the vertical profile of RH can be computed starting from the *in situ*

measurement of  $\theta$  and  $q$  at  $z = 60$  m in the following way. Successive height levels  $z_i$  are computed according to the hypsometric equation [Dutton, 1976, p. 64]

$$z_{i+1} = z_i + R_d \frac{T_v(z_i)}{g} \ln \left[ \frac{p(z_i) + dp}{p(z_i)} \right], \quad (1)$$

where  $R_d$  is the gas constant of dry air,  $T_v(z)$  is the virtual temperature (computed from  $\theta$  and  $q$ , which are assumed to be constant with height),  $g$  is acceleration due to gravity,  $p(z)$  is atmospheric pressure and  $dp$  is a sufficiently small pressure increment to capture cloud base with high accuracy. For each  $z$  the RH is determined by

$$\text{RH}(z) = \frac{q(z)}{q_s(T)}, \quad (2)$$

where the saturation water vapor mixing ratio is defined as

$$q_s(T) = \frac{0.622e_s(T)}{p(z) - e_s(T)} \quad (3)$$

and the saturation vapor pressure  $e_s(T)$  is computed according to Magnus' formula [Iribarne and Godson, 1973, p. 63]. The iterative procedure is carried out until  $q = q_s(T)$ , i.e. until cloud base is reached. Note that we do not make use of a lidar measure of cloud base as the relatively coarse range resolution of 39 m of the CART Raman lidar would introduce additional error in the determination of  $f(\text{RH})_\beta$ .

Combining the  $\text{RH}(z)$  profiles from the thermodynamic approach with profiles of the backscatter coefficient  $\beta(z)$  from the Raman lidar enables one to calculate

$$f(\text{RH})_\beta = \beta(\text{RH})/\beta(\text{RH}_{\text{ref}}) \quad (4)$$

which expresses the aerosol growth factor in terms of lidar backscatter at a given RH, relative to that at some lower  $\text{RH}_{\text{ref}}$ . Two and three parameter fits  $\beta(\text{RH})/\beta(\text{RH}_{\text{ref}}) = a[1 - (\text{RH}/100)]^{-b}$  [Kasten, 1969] and  $\beta(\text{RH})/\beta(\text{RH}_{\text{ref}}) = a[1 + b(\text{RH}/100)^c]$  [Kotchenruther and Hobbs, 1998], respectively, are applied to the data. We select either the two

or three parameter fit according to which provides the best  $\chi^2$  goodness of fit. The fit allows us to determine  $f(\text{RH})_\beta$  for specific RH values. Similarly these fit equations are also used to determine nephelometer  $f(\text{RH})_{\text{neph}}$ . To apply the method, the data set was first searched for cloud-capped, well-mixed cases. In order to determine whether the boundary layer was well-mixed we inspected available  $\theta$  and  $q$  profiles from radiosoundings, as well as the  $\beta$  profiles from lidar data. Furthermore, for the cases selected, it was ascertained that the  $\theta$  and  $q$  measurements at  $z = 60$  m were obtained above the surface layer and in the mixed layer. An additional data selection criterion was the accuracy of the cloud base determination using the thermodynamic assumptions. Simulations with a one-dimensional parcel model (see FM) show that a conservative estimate of cloud base lies in the first one-third of the region between the two points in the  $\beta(z)$  profile that exhibit the strongest gradient. This definition of cloud base was used in our study. Time periods that met all the requirements were used for further analysis.

## 4. Results

### 4.1. Lidar and nephelometer $f(\text{RH})$

A total number of 17 lidar time series (3 of which were measured during the IOP) ranging from ten minutes to one hour met the selection criteria and qualified for the comparison with nephelometer data. It should be noted that the data analyzed here were drawn from a subset of the entire 1998-2003 data set, used for a separate aerosol indirect effect study, and do not reflect the total number of cases during this time period. Figure 1 illustrates that nephelometer and lidar data are complementary for typical RH measurement ranges. Nephelometry measures  $f(\text{RH})$  for RH up to 85% and lidar extends the measurement range from 85% RH to close to saturation, i.e., beyond that which can currently be



achieved with nephelometry. To compare lidar and nephelometer-derived  $f(\text{RH})$  we first determine  $f(\text{RH})_\beta$  profiles for all 17 cases from the lidar backscatter data and the RH profiles, obtained from the thermodynamic assumptions (Figure 2). The backscatter data are normalized to  $\beta(84\%–86\% \text{ RH})$  (measurements of  $\beta$  are not always available at precisely 85%; for brevity we refer to this range as 85% RH) and the profiles are computed up to  $\text{RH}=98\%$ . Note the large range of  $f(\text{RH})_\beta$  values at 98% RH ( $\sim 1.5 - 4.2$ ), for the 17 cases under consideration. Backscatter data obtained at  $\text{RH}>98\%$  are not considered here because as RH approaches saturation even a small error in the determination of cloud base translates to a large error in RH and hence in  $f(\text{RH})_\beta$ . For example, an error of  $\pm 10 \text{ m}$  in  $z_{cb}$ , results in an error in  $f(\text{RH})_\beta$  of  $\pm \sim 12\%$  at  $\text{RH}=96.5\%$  and  $\pm \sim 50\%$  at 98.9% RH (FM).

For comparison with nephelometer-derived  $f(\text{RH})_{neph}$  for 85%/40% RH and at a wavelength of 450 nm we use the parameters for the fit to the lidar data (at 355 nm) up to 90%, 96% and 98% RH. We account for the different RH measurement ranges of the lidar and the nephelometer by normalizing the growth factors by their respective ranges,  $\Delta\text{RH}$ . (The wavelength difference is discussed in section 5.) Figure 3 shows the comparison between  $f(\text{RH})_{neph} (85\%/40\%)/\Delta\text{RH}_{neph}$  (hereafter referred to as  $f(\text{RH})'_{neph}$ ) and  $f(\text{RH})_\beta (90\%/85\%)/\Delta\text{RH}_\beta$  and indicates no correlation (correlation coefficient  $R=0.02$ ) between normalized lidar and nephelometer derived  $f(\text{RH})$  for these RH ranges (humidograph data were available for 11 out of the 17 cases). For an upper limit in RH of 96%,  $f(\text{RH})_\beta (96\%/85\%)/\Delta\text{RH}_\beta$  correlates well with  $f(\text{RH})'_{neph}$  ( $R=0.73$ ), as shown in Figure 4. We note that the values of  $f(\text{RH})_\beta (96\%/85\%)/\Delta\text{RH}_\beta$  are significantly larger than those of  $f(\text{RH})'_{neph}$ , reflecting the non-linear increase in growth with increasing RH as

illustrated in Figure 1. In Figure 5  $f(\text{RH})'_{neph}$  is compared to  $f(\text{RH})_{\beta}$  (98%/85%)/ $\Delta\text{RH}_{\beta}$ , with a correlation coefficient  $R=0.68$ . This shows that the lidar data contain hygroscopic growth information at increasingly larger RH, and over RH ranges that correspond to significant growth. We stress again that the confidence in the derived  $f(\text{RH})_{\beta}$  decreases as RH approaches saturation but this does not change the qualitative picture that emerges from Figs. 3–5.

## 4.2. Calculations based on in-situ aerosol data

To examine the factors controlling the relationship between lidar and nephelometer derived  $f(\text{RH})$  we analyze aerosol size and composition measurements from the DMA, TEOM and PILS-IC for the three days during the IOP that were deemed appropriate for this exercise. Figure 6 shows the mean aerosol size distributions (weighted by surface area) for May 8, 13 and 17 measured by the DMA during the time periods that correspond to the lidar and nephelometer measurements of  $f(\text{RH})$ . Superimposed on the figure is the scattering efficiency  $Q_{scat}$  at 450 nm for an aerosol with negligible absorption. The convolution of the surface size distribution with  $Q_{scat}$  represents the contribution of particles of different sizes to the total scattering. We interpolated the measured size distributions onto a finer grid to make them more suitable for model calculations as the Mie calculations behave non-monotonically with RH if the computational grid is too coarse. Figure 7 shows the aerosol mass concentration  $C$  for May 8, 13 and 17 in terms of mean total mass (TEOM), mean inorganic mass (PILS-IC), and the difference between the two; also shown is the mean inorganic fraction which we refer to as  $\epsilon$ . We use the aerosol size distribution in an aerosol model (FM) to compute backscatter  $\beta$  and total scattering  $\sigma_{sp}$  as a function of RH, thus allowing us to determine lidar and nephelometer-equivalent  $f(\text{RH})$ . The

aerosol model assumes a sulfate, soot and dust mixture with proportions constrained by the measured inorganic fraction  $\epsilon$  and the measured single scattering albedo  $\omega_o$ . Without knowledge of the non-inorganic aerosol, we make a rough approximation that it is insoluble, i.e., that  $\epsilon$  represents the soluble mass fraction. We then perform calculations with a range of  $\epsilon$  values to account for the likelihood that some of the non-inorganic fraction is soluble.

The normalized growth factors, as computed from the *in situ* size distribution and composition data for May 8, 13 and 17, are superimposed as colored symbols in Figure 4. For this comparison we focus on the relationship between  $f(\text{RH})_\beta (96\%/85\%)/\Delta\text{RH}_\beta$  (hereafter termed  $f(\text{RH})'_\beta$ ) and  $f(\text{RH})'_{\text{neph}}$ , as we have more confidence in the data from this RH range, and because the correlation between the lidar and nephelometer is the greatest. On May 8 the normalized measured lidar and nephelometer  $f(\text{RH})$  compare well with the normalized  $f(\text{RH})$  computed from the *in situ* data. As noted above, the fraction of soluble material is uncertain and so the mean values are perturbed to the minimum and maximum values observed during the time period. These variations in  $\epsilon$  have the effect of increasing (decreasing) both the lidar and nephelometer equivalent  $f(\text{RH})$  values for increasing (decreasing)  $\epsilon$  (Figure 4) but their positions do not deviate very much from the general trend because changes in  $\epsilon$  affect particle scattering and backscatter to similar degrees.

In Figure 8 both the normalized lidar backscatter ( $\beta_{\text{norm}}$ ) and normalized nephelometer total scattering  $\sigma_{\text{norm}}$  from measurements (circles) and the aerosol model calculations (stars) are shown. Note that the measured and calculated humidified nephelometer total scattering coefficients are normalized by the dry (40 %) total scattering coefficient whereas

the lidar backscatter coefficients are normalized by  $\beta(85\% \text{ RH})$ . Because of this different normalization procedure we stress that only the slopes, and not absolute values, are to be compared. Both measured and computed  $\beta_{norm}$  and  $\sigma_{norm}$  profiles show similar slopes for May 8, hence the good agreement in  $f(\text{RH})'_\beta$  and  $f(\text{RH})'_{neph}$  (Figure 4). On May 13 the normalized  $f(\text{RH})$  computed from *in situ* data compares well with the measured nephelometer  $f(\text{RH})'_{neph}$ , but it differs from the measured lidar  $f(\text{RH})'_\beta$ . Figure 8 clearly shows the steeper slope in the measured profile of  $\beta_{norm}$  when compared to  $\beta_{norm}$  computed from *in situ* data. We suspect that the arrival of a frontal passage might have caused the discrepancy between values measured with lidar and computed from *in situ* data. Figures 9(a) and 9(b) show the measured time series of the total scattering coefficient  $\sigma_{sp}$  and absorption coefficient  $\sigma_{ap}$ , respectively. The figures indicate a rapid change in aerosol size and composition starting at  $\sim 1320$  UT until  $\sim 1720$  UT, which encompasses the lidar and nephelometer measurement period from 1620–1650 UT. Due to this rapid change in aerosol properties the surface layer and the mixed layer aerosol might have differed substantially, which could have contributed to the difference in  $f(\text{RH})'_\beta$  and  $f(\text{RH})'_{neph}$ . For May 17 the measured lidar  $f(\text{RH})'_\beta$  and the computed  $f(\text{RH})'_\beta$  compare well (Figures 4 and 8). However, the slopes for the measured and computed normalized nephelometer scattering coefficients differ (Figure 8). This is reflected in a disagreement of the respective  $f(\text{RH})'_{neph}$  values (Figure 4).

#### 4.3. $f(\text{RH})$ , $\tilde{a}$ and $\omega_o$

As this data set covers a broad range of atmospheric aerosol conditions (Figure 2) it is instructive to investigate the relationship between  $f(\text{RH})$  and the Ångström exponent  $\tilde{a}$ , a parameter closely related to the size distribution of the aerosol population. In 14

of the 17 cases studied here nephelometer data at 450 nm and 700 nm were available to compute  $\bar{a}$ . In Figure 10,  $f(\text{RH})'_\beta$  (which is qualitatively similar to  $f(\text{RH})'_{\text{neph}}$ ; Figure 4) is plotted against  $\bar{a}$ . The data indicate that  $f(\text{RH})'_\beta$  tends to increase with increasing  $\bar{a}$  although the correlation is weak ( $R=0.15$ ). This qualitative trend can be explained by the fact that at large  $\bar{a}$ , there is a preponderance of small particles with low scattering efficiency. The effect of increasing RH is to allow these particles to grow to sizes at which they are more efficient scatterers. *Sheridan et al.* [2001] found, based on analysis of *in situ* data collected at SGP in 1999, that aerosols containing higher fractions of smaller particles show larger hygroscopic growth factors. This is consistent with the trend for  $f(\text{RH})'_\beta$  vs  $\bar{a}$  found here.

It is likely that  $f(\text{RH})$  is closely tied to aerosol composition. For example, the water vapor uptake by inorganic salts is typically higher than for dicarboxylic organic acids [*Saxena and Hildemann*, 1996]. Also, mixtures of inorganic and organic material may exhibit suppressed deliquescence relative humidity [*Raymond and Pandis*, 2002]. Since for non-IOP days complete aerosol composition data are unavailable, and because we expect the amount of organic material (particularly black carbon) to affect both water vapor uptake and light absorption, we use the single scattering albedo  $\omega_o$  as a composition proxy to explore the effect of composition on  $f(\text{RH})$ . In Figure 11  $f(\text{RH})'_\beta$  is plotted as a function of  $\omega_o$  for 8 out of a total of 17 cases that were available (only a limited number of absorption measurements, required for the determination of  $\omega_o$ , was available due to instrument downtime). The range of  $\omega_o$  is 0.922 to 0.980. The data show a weak positive correlation ( $R=0.43$ ), but due to the sparseness of the data a clear trend cannot be deduced. We refer again to the study by *Sheridan et al.* [2001] who showed that aerosols

containing higher fractions of more strongly absorbing particles exhibit lower hygroscopic growth factors. *Delene and Ogren* [2002] studied the behavior of  $\omega_o$  as a function of the aerosol light scattering coefficient for data collected over a three and a half year period at the SGP site. They found that  $\omega_o$  increased with increasing aerosol light scattering coefficient. However, future studies will be required to clarify the relationship between  $f(\text{RH})$  and  $\omega_o$ .

## 5. Discussion

### 5.1. Assessment of the method

The consistency between the measurements of  $f(\text{RH})'_\beta$  and  $f(\text{RH})'_{neph}$  described above provides confidence in the lidar methodology for studying aerosol hygroscopic growth. Nevertheless, a number of issues need to be factored in to these comparisons. The importance of these will vary depending on the particular aerosol conditions that present themselves. The following important caveats should be considered:

- (a) a lidar measures  $180^\circ$  backscatter whereas a nephelometer measures total scattering. FM addressed this issue and showed with model calculations for marine type aerosol that for  $\text{RH} < \sim 95\%$ ,  $f(\text{RH})_\beta \simeq f(\text{RH})_{neph}$ . However, the agreement may vary for different aerosol size distribution and composition;
- (b) the two instruments measure over different RH ranges. We note that the general relationship between  $f(\text{RH})'_\beta$  and  $f(\text{RH})'_{neph}$  is closely related to the selected RH ranges for each instrument. Nephelometer  $f(\text{RH})$  is commonly computed over a RH range from 40% to 85% and this convention has been adopted here. In the case of lidar we investigate three RH ranges to compute  $f(\text{RH})'_\beta$  (90%, 96% and 98%) and find good correlation with  $f(\text{RH})'_{neph}$  for both upper limits 96% and 98%;

(c) the lidar measures at 355 nm whereas the nephelometer measures at 450 nm. From model calculations we find that the effect of the wavelength difference on backscatter and total scattering is closely related to the aerosol size distribution and composition. Based on extensive calculations (not shown) we draw the following broad generalizations: (i) the more absorbing the particles, the larger the total scattering relative to the backscatter (and hence the larger  $f(\text{RH})_{\text{neph}}$  relative to  $f(\text{RH})_{\beta}$ ); (ii) the difference between backscatter and total scattering due to the wavelength difference tends to be less significant for smaller particles. For a more quantitative assessment, these biases should be considered on a case-by-case basis.

(d)  $f(\text{RH})_{\beta}$  is based on lidar profiling of the mixed layer, whereas  $f(\text{RH})_{\text{neph}}$  is determined from in-situ ground based measurements in the surface layer. The surface layer is in general affected by surface processes on shorter time scales than the mixed layer. Apparently this did not significantly affect the current analysis except for the IOP day May 13 when the arrival of a frontal passage may have resulted in different aerosol properties within the surface layer and in the mixed layer. The fact that time-averaged quantities were used rather than instantaneous measurements may have alleviated this problem;

(e) cloud base height has been determined here based on thermodynamic arguments rather than from lidar backscatter, as the Raman lidar range resolution is too coarse for this purpose. To obtain high accuracy in cloud base determination using thermodynamic arguments it is important that the micrometeorological parameters be measured in the mixed layer, as was done here. Ideally, however, a lidar with high spatial resolution (order of meters) should be used as an additional measure of cloud base (see FM). Furthermore, combined Raman lidar and Atmospheric Emitted Radiance Interferometer

(AERI) and Geostationary Operational Environmental Satellite (GOES) measurements of RH [Turner *et al.*, 2000] could be included in future analyses. Comparison between lidar- and thermodynamically-derived cloud base will provide a stronger criterion for well-mixed conditions and provide greater confidence in  $f(\text{RH})_\beta$  at RH close to saturation.

## 6. Summary

A lidar technique that employs thermodynamic assumptions for well-mixed, cloud-capped boundary layers has been used to compute profiles of the hygroscopic growth factor  $f(\text{RH})$  for ambient, unperturbed atmospheric conditions. The lidar-derived  $f(\text{RH})$  over the range 85% to 96% RH correlate well with the growth factors from a collocated ground-based humidified nephelometer (40% RH to 85% RH). To our knowledge, this is the first observational evidence of the consistency between these two methods of deriving  $f(\text{RH})$ . The slopes of the growth curves reflect the fact that the growth over the range 85% RH to 96% RH is much stronger than over the range 40% to 85%. The measurements were corroborated by a comparison of measured  $f(\text{RH})$  with those computed from *in situ* measurement of size distribution and composition for three cases during the May 2003 IOP.

We have investigated the possible relationship between aerosol size distribution and  $f(\text{RH})_\beta$  using the Ångström exponent as a proxy for size distribution. The data suggest that  $f(\text{RH})_\beta$  (96%/85%) increases with increasing  $\text{\AA}$ . A plausible explanation is that at high  $\text{\AA}$ , the dominance of smaller particles that are inefficient scatterers yields low backscatter, and their growth due to uptake of water vapor allows them to scatter more efficiently. At low  $\text{\AA}$ , the growth of the larger particles, that are already efficient scatterers, has less effect on  $f(\text{RH})_\beta$ . Preliminary investigation of the effect of aerosol



composition (represented by the single-scattering albedo) shows a weak positive trend between  $f(\text{RH})_\beta$  (96%/85%) and  $\omega_o$ , but due to the rather small number of data points analyzed, we cannot draw any conclusions regarding the suitability of  $\omega_o$  as a proxy for aerosol composition. Further analyses are required to determine whether there is a clear relationship between  $f(\text{RH})_\beta$  and  $\omega_o$ .

The current study extends the prior demonstrations of this technique by *Wulfmeyer and Feingold* [2000] and FM and provides further confidence that lidar can be a useful tool for measurement of aerosol growth, particularly at  $\text{RH} > 85\%$ . It is suggested that measurements of this kind will benefit greatly from higher lidar range resolution (on the order of meters) which will increase the accuracy of retrievals at RH approaching saturation.

### Acknowledgments

The data used for this study were obtained from the Atmospheric Radiation Measurement (ARM) Program sponsored by the U.S. Department of Energy, Environmental Sciences Division. The authors thank the awarding agency as well as ARM staff for maintaining the instrumentation and the ARM database. MP was supported by the NOAA Postdoctoral Program in Climate and Global Change, administered by the University Corporation for Atmospheric Research. GF was partially supported by the Biological and Environmental Research program (BER), U.S. Department of Energy, grant number DE-A103-02ER63324. We acknowledge the role of ARM's Climate Research Facility in supporting the acquisition of surface aerosol data.

## References

- Boucher, O. and T. L. Anderson, General circulation model assessment of the sensitivity of direct climate forcing by anthropogenic sulfate aerosols to aerosol size and chemistry. *J. Geophys. Res.*, *100*, 26117- 26134, 1995.
- Brechtel, F. J. and S. M. Kreidenweis, Predicting particle critical supersaturation from hygroscopic growth measurements in the humidified TDMA. Part II: Laboratory and ambient studies. *J. Atmos. Sci.*, *57*, 1872-1887, 2000.
- Charlson, R. J., S. E. Schwartz, J. M. Hales, R. D. Cess, J. A. Oakley Jr., J. E. Hansen, and D. J. Hofmann, Climate forcing by anthropogenic aerosols, *Science*, *255*, 423-430, 1992.
- Covert, D. S., R. J. Charlson, and N. C. Ahlquist, A study of the relationship of chemical composition and humidity to light scattering by aerosols, *J. Appl. Meteorol.*, *11*, 968-976, 1972.
- Covert, D. S. and J. Heintzenberg, Size distribution and chemical properties of aerosol at Ny Alesund, Svalbard. *Atmos. Environ.*, *27A*, 2989-2997, 1993.
- Delene, D. J. and J. A. Ogren, Variability of aerosol optical properties at four North American surface monitoring sites, *J. Atmos. Sci.*, *59*, 1135-1150, 2002.
- Dutton, J. A., *Dynamics of atmospheric motion*, 617 pp., Dover, New York, 1976.
- Feingold, G. and B. Morley, Aerosol hygroscopic properties as measured by lidar and comparison with in situ measurements. *J. Geophys. Res.*, *108*, doi:10.1029/2002JD002842, 2003.

- Ferrare, R. A., S. H. Melfi, D. N. Whiteman, K. D. Evans, M. Poellot, and Y. J. Kaufman, Raman lidar measurements of aerosol extinction and backscattering 2. Derivation of aerosol real refractive index, single-scattering albedo, and humidification factor using Raman lidar and aircraft size distribution measurements. *J. Geophys. Res.*, *103*, 19673-19689, 1998.
- Goldsmith, J. E. M., S. E. Bisson, H. B. Blair, and D. D. Turner, Turn-key Raman lidar for profiling atmospheric water vapor, clouds, and aerosols. *Appl. Opt.*, *37*, 4979-4990, 1998.
- Iribarne, J. V. and W. L. Godson, *Atmospheric Thermodynamics*, 222 pp., Reidel, Dordrecht, 1973.
- Kasten, F., Visibility forecast in the phase of pre-condensation. *Tellus*, *21*, 631-635, 1969.
- Kotchenruther, R. A. and P. V. Hobbs, Humidification factors of aerosols from biomass burning in Brazil. *J. Geophys. Res.*, *103*, 32081-32089, 1998.
- Kotchenruther, R. A., P. V. Hobbs, and D. A. Hegg, Humidification factors for atmospheric aerosols off the mid-Atlantic coast of the United States. *J. Geophys. Res.*, *104*, 2239-2251, 1999.
- Malm, W. C., D. E. Day, S. M. Kreidenweis, J. L. Collett, and T. Lee, Humidity-dependent optical properties of fine particles during the Big Bend Regional Aerosol and Visibility Observational Study. *J. Geophys. Res.*, *108*, 4279, doi:10.1029/2002JD002998, 2003.
- McInnes, L., M. Bergin, J. Ogren, and S. Schwartz, Apportionment of light scattering and hygroscopic growth to aerosol composition. *Geophys. Res. Lett.*, *25*, 513-516, 1998.

- McMurry, P. H. and M. R. Stolzenburg, On the sensitivity of particle size to relative humidity for Los Angeles aerosols. *Atmos. Environ.*, *23*, 497-507, 1989.
- Orsini, D. A., Y. Ma, A. Sullivan, B. Sierau, K. Baumann, and R. J. Weber, Refinements to the particle-into-liquid sampler (PILS) for ground and airborne measurements of water soluble aerosol composition. *Atmos. Environ.*, *37*, 1243-1259, 2003.
- Raymond, T. M. and S. N. Pandis, Cloud activation of single-component organic aerosol particles, *J. Geophys. Res.*, *107*, 4787, doi:10.1029/2002JD002159, 2002.
- Sheridan, P. J., D. J. Delene, and J. A. Ogren, Four years of continuous surface aerosol measurements from the Department of Energy's Atmospheric Radiation Measurement Program Southern Great Plains Cloud and Radiation Testbed site. *J. Geophys. Res.*, *106*, 20735-20747, 2001.
- Turner, D. D., W. F. Feltz, and R. A. Ferrare, Continuous water vapor profiles from operational ground-based active and passive remote sensors, *Bull. Amer. Meteor. Soc.*, *81*, 1301-1317, 2000.
- Turner, D. D., R. A. Ferrare, L. A. Heilman, W. F. Feltz, and T. P. Tooman, Automated retrievals of aerosol extinction coefficient from Raman lidar, *J. Atmos. Oceanic Tech.*, *19*, 37-50, 2002.
- Twomey, S., Pollution and the planetary albedo, *Atmos. Environ.*, *8*, 1251-1256, 1974.
- Saxena, P. and L. M. Hildemann, Water-soluble organics in atmospheric particles: A critical review of the literature and application of thermodynamics to identify candidate compounds, *J. Atmos. Chem.*, *24*, 57-109, 1996.

- Vogelmann, A. M., P. J. Flatau, M. Szczodrak, K. M. Markowicz, and P. J. Minnett, Observations of large aerosol infrared forcing at the surface. *Geophys. Res. Lett.*, *30*, 1655, doi:10.1029/2002GL016829, 2003.
- Wulfmeyer, V. and G. Feingold, On the relationship between relative humidity and particle backscattering coefficient in the marine boundary layer determined with differential absorption lidar. *J. Geophys. Res.*, *105*, 4729-4741, 2000.

## Figure captions

Figure 1. Schematic illustrating the measurement range of nephelometer and lidar and the enhancement in scattering that aerosol undergoes for each respective RH range.

Figure 2. Model parameter fit of  $f(\text{RH})_\beta (= \beta(\text{RH})/\beta(85\%))$  to experimental data for RH ranging from 85% to 98%. The 17 cases that were available for analysis are shown. Routine measurement period data are shown as black lines and the IOP data are color coded (red: May 8; green: May 13; blue: May 17)

Figure 3. Comparison of the normalized  $f(\text{RH})_\beta (90\%/85\%)/\Delta\text{RH}_\beta$  (where  $\Delta\text{RH}_\beta = 5\%$ ) with  $f(\text{RH})_{\text{neph}} (85\%/40\%)/\Delta\text{RH}_{\text{neph}}$  (where  $\Delta\text{RH}_{\text{neph}} = 45\%$ ). Circles denote data obtained during the routine measurement period and square symbols represent data obtained during the IOP (red: May 8; green: May 13; blue: May 17). Error bars denote one standard deviation between the measured  $f(\text{RH})$  and the  $f(\text{RH})$  determined from the fit parameters.

Figure 4. Comparison of the normalized  $f(\text{RH})_\beta (96\%/85\%)/\Delta\text{RH}_\beta$  (where  $\Delta\text{RH}_\beta = 11\%$ ) with  $f(\text{RH})_{\text{neph}} (85\%/40\%)/\Delta\text{RH}_{\text{neph}}$ . Symbols and error bars as in Figure 3. Additional symbols represent data computed with an aerosol model. Diamonds represent results obtained for mean inorganic fraction. Upward (downward) pointing triangles were obtained for maximum (minimum) inorganic fraction during time period of interest.

Figure 5. Comparison of the normalized  $f(\text{RH})_\beta (98\%/85\%)/\Delta\text{RH}_\beta$  (where  $\Delta\text{RH}_\beta = 13\%$ ) with  $f(\text{RH})_{\text{neph}} (85\%/40\%)/\Delta\text{RH}_{\text{neph}}$ . Symbols and error bars as in Figure 3.

Figure 6. Mean surface size distributions measured on May 8 (red), 13 (green) and 17 (blue) during time periods that correspond to the lidar and nephelometer measurement

periods (May 8: 15:10–15:50 UT, May 13: 16:20–16:50 UT; May 17: 18:10–18:30 UT). The black line represents the scattering efficiency  $Q_{scat}$  at 450 nm for a nonabsorbing aerosol.

Figure 7. Left column: Aerosol composition  $C$  in terms of total mass (solid line), inorganic fraction (dashed line) and the difference between the two (dashed-dotted line); Right column: inorganic fraction  $\epsilon$ ; Top row: May 8, middle row: May 13 and bottom row: May 17

Figure 8. Normalized measured lidar and nephelometer backscatter and total scattering coefficients (circles) and normalized computed backscatter and total scattering coefficients from aerosol model (stars). The normalized backscatter coefficients  $\beta_{norm}$  are shown in the left column and the normalized total scattering coefficients  $\sigma_{norm}$  are shown in the right column.

Figure 9. Time series of (a) total scattering coefficient  $\sigma_{sp}$  at 450 nm and (b) absorption coefficient  $\sigma_{ap}$  at 565 nm for May 13.

Figure 10.  $f(RH)_\beta$  (96%/85%) as a function of Ångström exponent  $\mathring{a}$  as determined from nephelometer at 700 nm and 450 nm. The error bars for  $\mathring{a}$  represent one standard deviation from the mean in  $\mathring{a}$  over the respective measurement period. Error bars for  $f(RH)_\beta$  (96%/85%) denote one standard deviation between the measured  $f(RH)_\beta$  and the  $f(RH)_\beta$  determined from the fit parameters. Symbols are as in Figure 3.

Figure 11.  $f(RH)_\beta$  (96%/85%) as a function of single scattering albedo  $\omega_o$  as determined from the nephelometer at 450 nm and the light absorption photometer. The error bars for  $\omega_o$  represent one standard deviation from the mean in  $\omega_o$  over the respective

measurement period. Error bars for  $f(\text{RH})_\beta$  (96%/85%) denote one standard deviation between the measured  $f(\text{RH})_\beta$  and the  $f(\text{RH})_\beta$  determined from the fit parameters. Symbols are as in Figure 3.



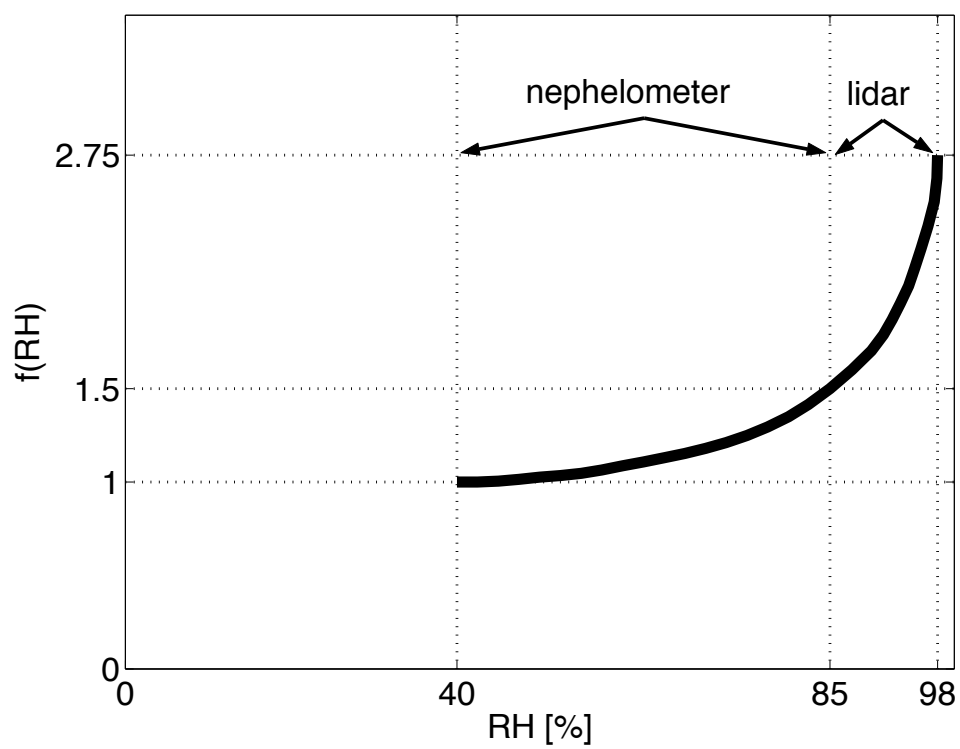


Figure 1.

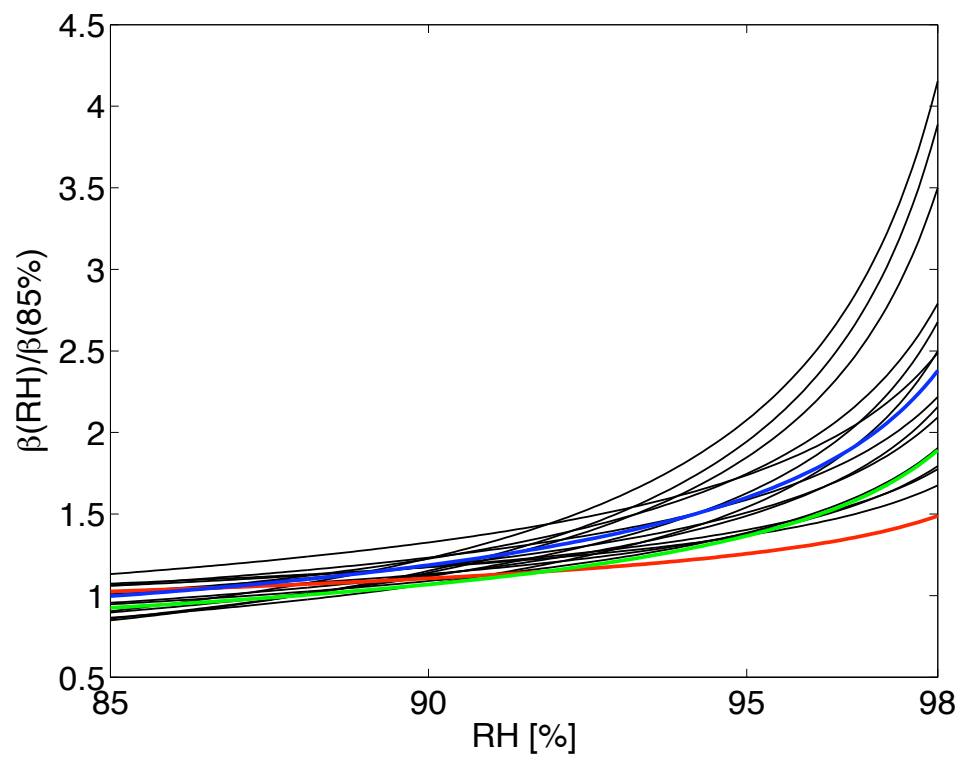


Figure 2.

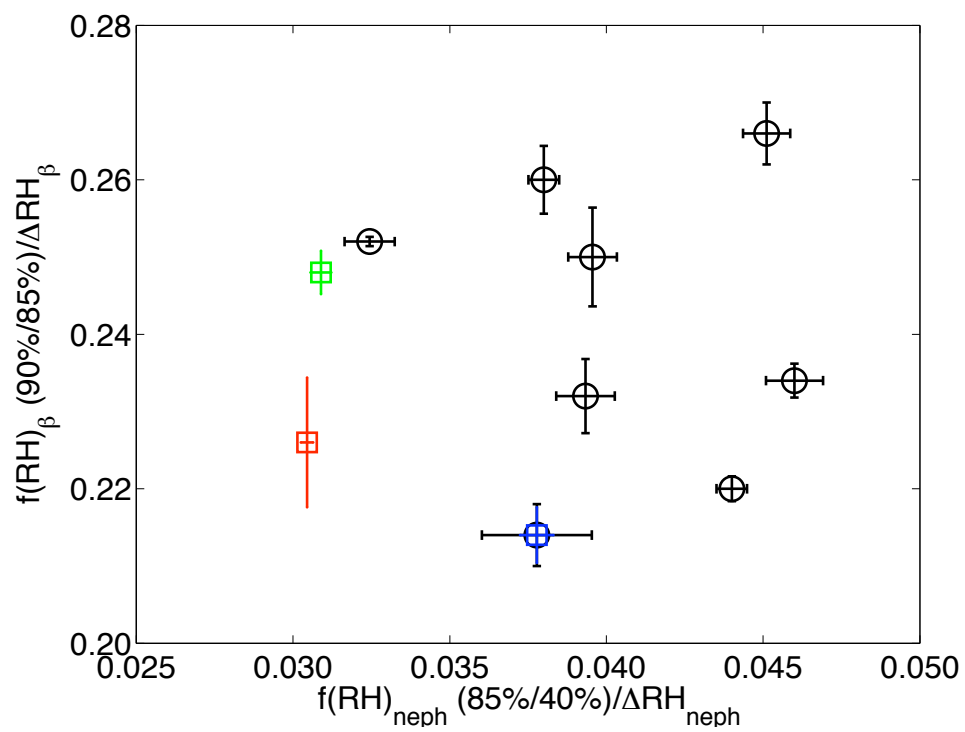


Figure 3.

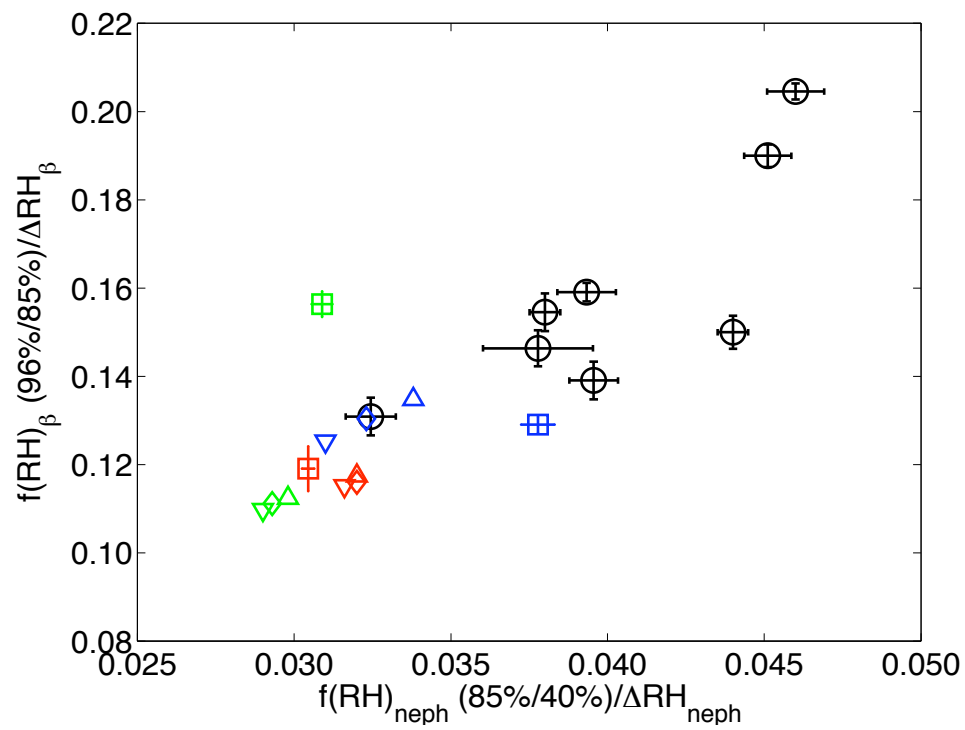


Figure 4.

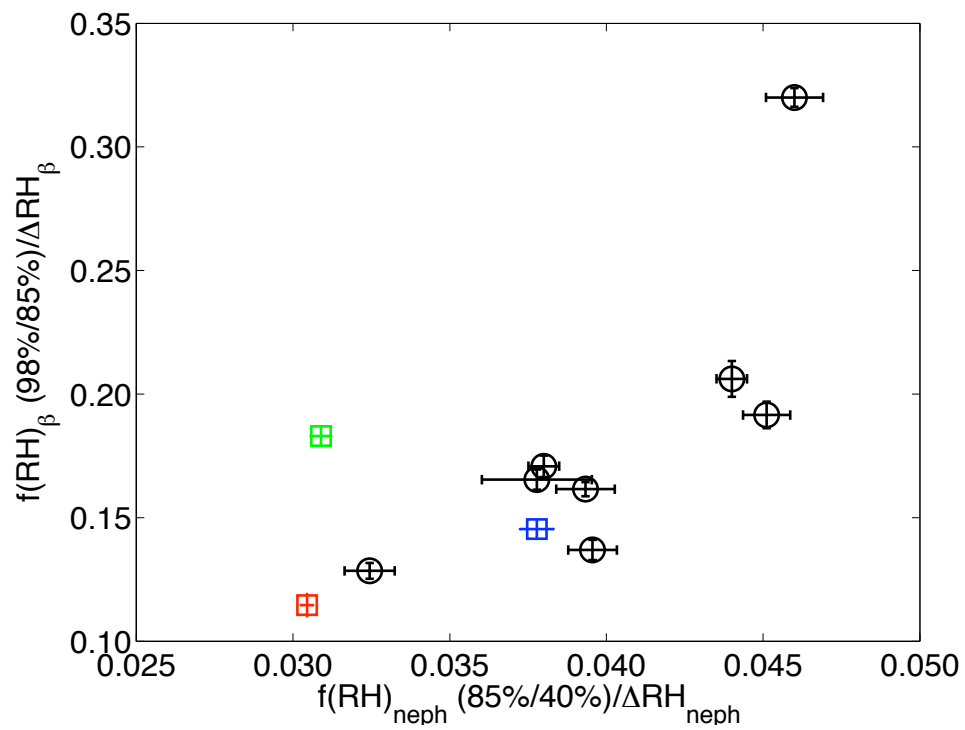


Figure 5.

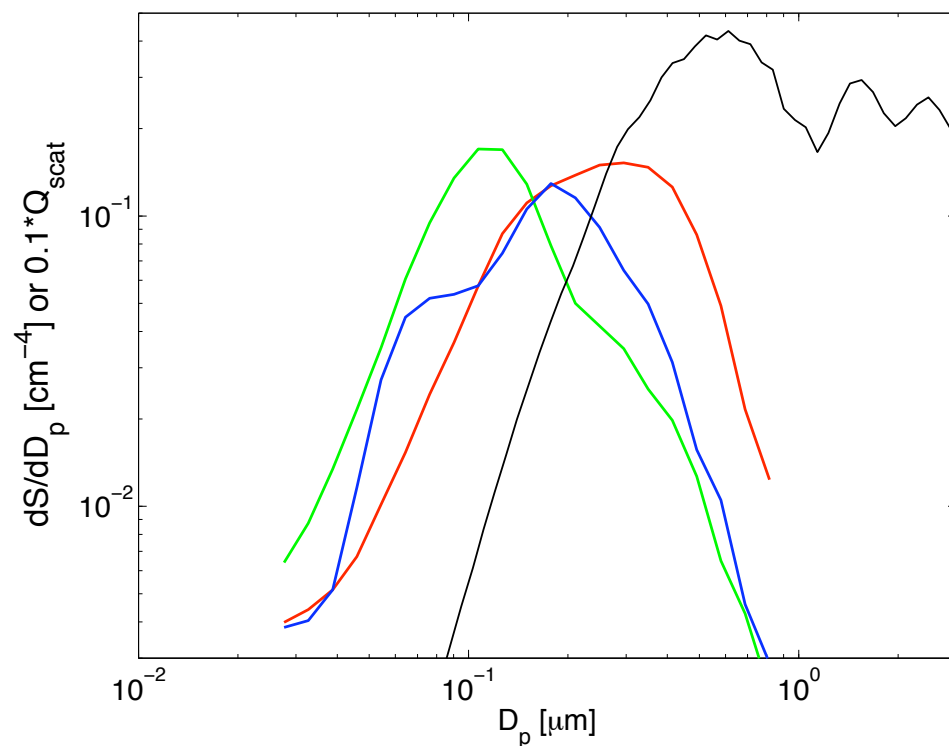


Figure 6.

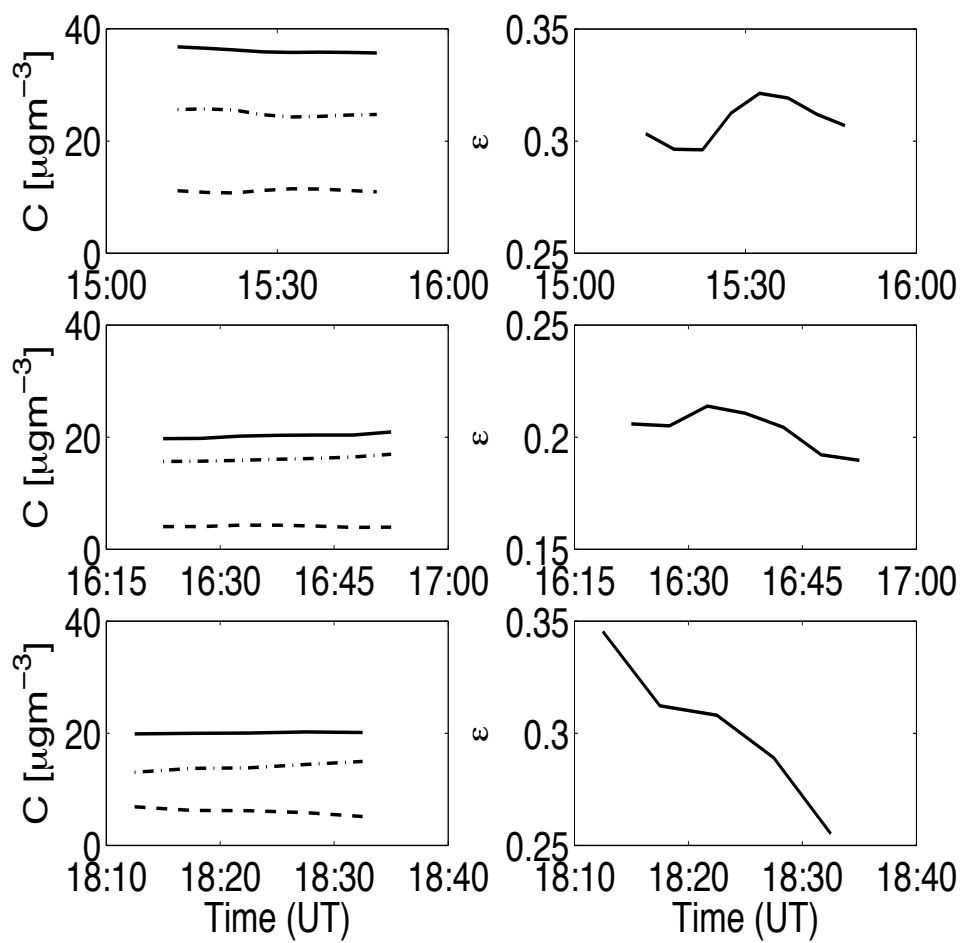


Figure 7.

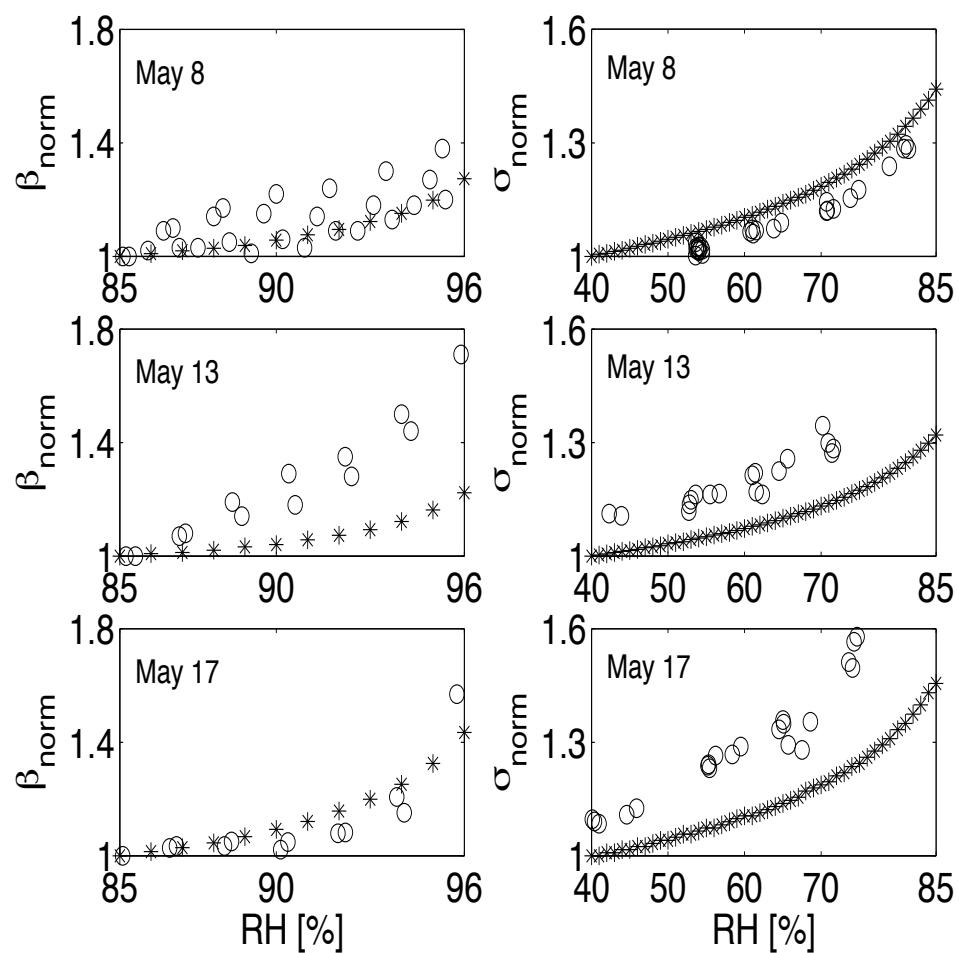


Figure 8.



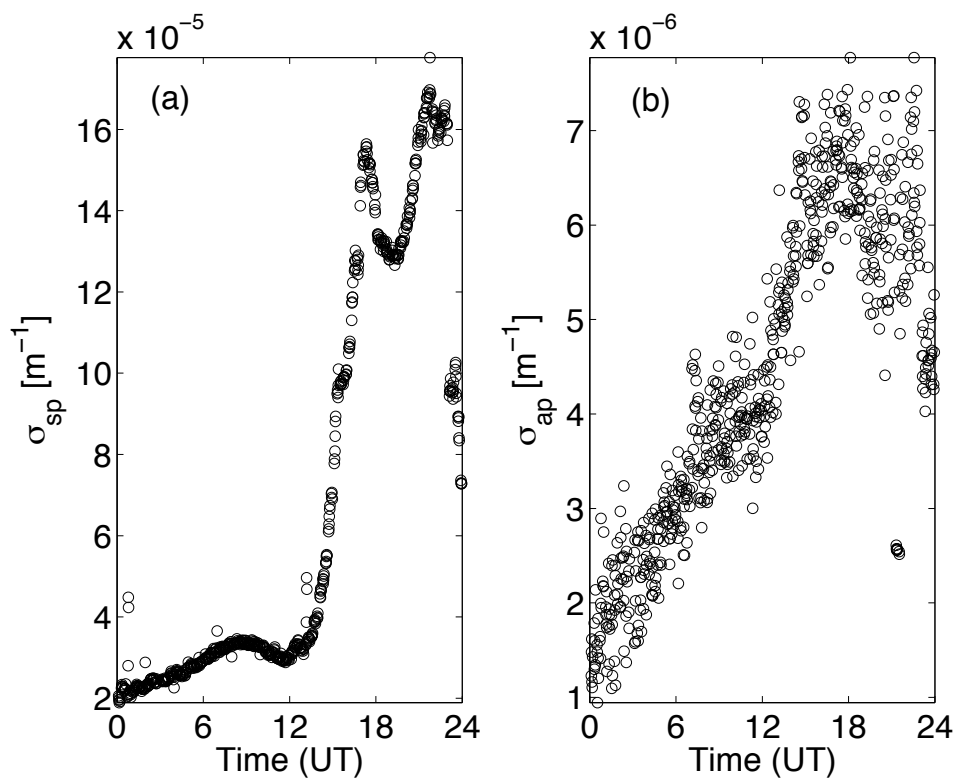


Figure 9.

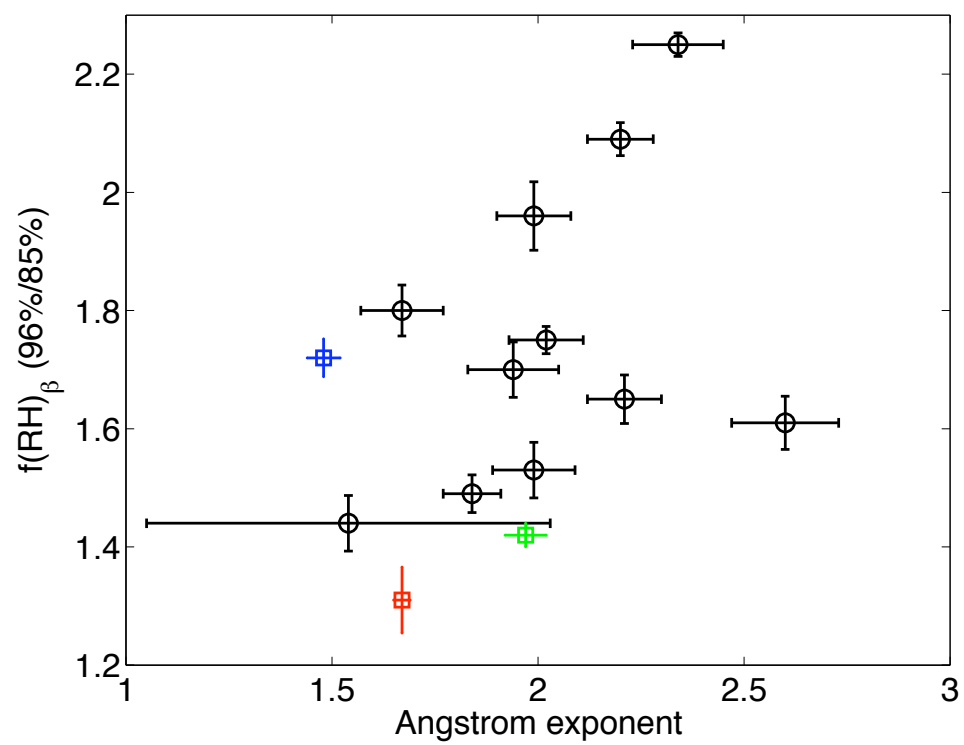


Figure 10.

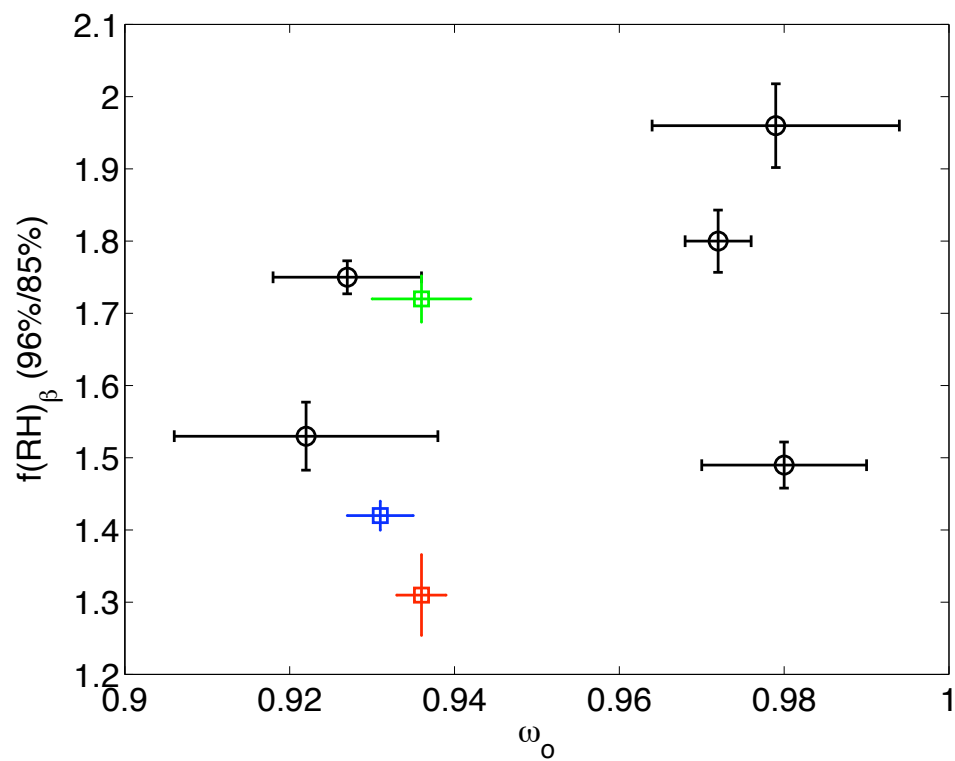


Figure 11.